Article

A Novel Gold Film-Coated V-Shape Dual-Core Photonic Crystal Fiber Polarization Beam Splitter Covering the E + S + C + L + U Band

Yuwei Qu [1], Jinhui Yuan [1,2,*], Shi Qiu [1], Xian Zhou [2], Feng Li [3], Binbin Yan [1], Qiang Wu [4,5], Kuiru Wang [1], Xinzhu Sang [1], Keping Long [2] and Chongxiu Yu [1]

[1] State Key Laboratory of Information Photonics and Optical Communications, Beijing University of Posts and Telecommunications, Beijing 100876, China; laigen007@163.com (Y.Q.); qiushi@bupt.edu.cn (S.Q.); yanbinbin@bupt.edu.cn (B.Y.); krwang@bupt.edu.cn (K.W.); xzsang@bupt.edu.cn (X.S.); cxyu@bupt.edu.cn (C.Y.)

[2] Research Center for Convergence Networks and Ubiquitous Services, University of Science & Technology Beijing (USTB), Beijing 100083, China; zhouxian219@ustb.edu.cn (X.Z.); longkeping@ustb.edu.cn (K.L.)

[3] Photonics Research Centre, Department of Electronic and Information Engineering, The Hong Kong Polytechnic University, Hung Hom, Hong Kong; enlf@polyu.edu.hk

[4] Department of Physics and Electrical Engineering, Northumbria University, Newcastle upon Tyne NE1 8ST, UK; krwang@bupt.edu.cn

[5] Key Laboratory of Nondestructive Test (Ministry of Education), Nanchang Hangkong University, Nanchang 330063, China

* Correspondence: yuanjinhui81@bupt.edu.cn

Abstract: In this paper, a novel gold film-coated V-shape dual-core photonic crystal fiber (V-DC-PCF) polarization beam splitter (PBS) based on surface plasmon resonance effect is proposed. The coupling lengths of the X-polarization (X-pol) and Y-polarization (Y-pol) and the corresponding coupling length ratio of the proposed V-DC-PCF PBS without gold film and with gold film are compared. The fiber structure parameters and thickness of the gold film are optimized through investigating their effects on the coupling lengths and coupling length ratio. As the propagation length increases, the normalized output powers of the X-pol and Y-pol of the proposed V-DC-PCF PBS at the three wavelengths 1.610, 1.631, and 1.650 μm are demonstrated. The relationships between the extinction ratio (*ER*), insertion loss (*IL*) and wavelength for the three splitting lengths (*SLs*) 188, 185, and 182 μm are investigated. Finally, it is demonstrated that for the proposed V-DC-PCF PBS, the optimal *SL* is 188 μm, the *ILs* of the X-pol and Y-pol are less than 0.22 dB, and the splitting bandwidth (*SB*) can cover the E + S + C + L + U band. The proposed V-DC-PCF PBS has the ultra-short *SL*, ultra-wide *SB*, and ultra-low *IL*, so it is expected to have important applications in the laser, sensing, and dense wavelength division multiplexing systems.

Keywords: V-shape dual-core photonic crystal fiber; polarization beam splitter; surface plasmon resonance effect; extinction ratio; insertion loss

1. Introduction

Since the first photonic crystal fiber (PCF) was fabricated by Russell et al. in 1996 [1], PCFs have been investigated extensively and applied in different optical fields, such as fiber laser, sensing, optical communication, and so on [2–8]. At present, the PCF-based optical devices, including polarization beam splitter (PBS), polarization filter, modulator, etc., have become the indispensable components in the all-fiber optical systems [9–14].

In recent years, the dual-core PCF (DC-PCF) PBS based on the coupled mode theory has been widely investigated [15–19]. In 2016, Zi et al. reported a simple DC-PCF PBS, whose splitting lengths (*SLs*) are 249 and 506 μm and splitting bandwidths (*SBs*) are 17 and 12 nm at wavelengths 1.55 and 1.31 μm, respectively [20]. In the same year, Wang et al. proposed a liquid crystal-filled DC-PCF PBS, whose *SL* is 890.5 μm and *SB* covers the

S + C + L band [21]. In 2017, He et al. designed an octagonal lattice DC-PCF PBS with the five elliptical air holes, whose *SL* is 105 μm and *SB* covers the S + C + L band [22]. In 2017, Wang et al. demonstrated a surface plasmon resonance (SPR) effect-based DC-PCF PBS filled with elliptical gold wire, whose *SL* is 1.079 mm and *SB* only covers the C band [23]. In 2018, Wang et al. achieved a short DC-PCF PBS with the liquid filled in the central and two elliptical air holes, whose *SL* is 78 μm and *SB* only covers the C band [24]. In 2019, Lou et al. investigated an ultrashort SPR effect-based DC-PCF PBS coated with gold film, whose *SL* is only 47.26 μm and *SB* cannot cover the C band [25]. From the previous works, the performances of the DC-PCF PBS can be obviously improved by introducing the elliptical air holes, changing the lattice arrangement of air holes, and selectively filling or coating the air holes with the liquid crystal, liquid, metal wire, and metal film.

Up to now, the fabrication technology of the PCFs with the circular air holes arranged in a hexagonal lattice has been developed more mature [26–32]. Many fabrication methods have been reported, including stack-and-draw, 3D printing, femtosecond laser drilling, etc. [33–39]. In contrast, it is more difficult to fabricate the PCFs when the air holes are arranged in the rectangle and octagonal shapes or the elliptical air holes exist. Especially when selectively filling the metal wire or coating the metal film into the air holes of the PCFs, the difficulty of fabrication is further increased. Since Sazio et al. and Russell et al. Firstly demonstrated the gold film-coated PCF in 2006 [40] and gold wire-filled PCF in 2008 [41], respectively, there are some reports on fabricating the gold film-coated and gold wire-filled PCFs by different methods [42–48]. At present, it is becoming a research hotspot to design and fabricate the gold film-coated or gold wire-filled DC-PCF PBS which has the hexagonal arrangement of circular air holes.

In this paper, we propose a novel gold film-coated V-shape DC-PCF (V-DC-PCF) PBS based on the SPR effect. We compare the coupling lengths (*CLs*) of the X-polarization (X-pol) and Y-polarization (Y-pol) and the coupling length ratio (*CLR*) when the proposed V-DC-PCF PBS is coated with and without gold film. At the three wavelengths 1.610, 1.631, and 1.650 μm, the normalized output powers of the X-pol and Y-pol of the V-DC-PCF PBS are demonstrated when the propagation length increases. For the three splitting lengths (*SLs*) 188, 185, and 182 μm, the extinction ratio (*ER*) and insertion loss (*IL*) of the proposed V-DC-PCF PBS are investigated. Finally, we obtain a V-DC-PCF PBS with good performances, whose optimal *SLs* is 188 μm, *ILs* of the X-pol and Y-pol are less than 0.22 dB, and *SB* can cover the E + S + C + L + U band.

2. Design of the V-DC-PCF PBS

The three-dimensional and cross-sectional structures of the proposed V-DC-PCF PBS are shown in Figure 1a,b, respectively. From Figure 1a,b, the substrate material is silica, the air holes are arranged in a hexagonal lattice, and the hole to hole pitch is Λ. The most central air hole with the diameter of d_1 is coated with the gold film, which has a thickness of *t*. When the light energy is propagated inside the V-DC-PCF coated with gold film, the free electrons on the gold film surface interact with the incident light field, generating the SPR and exciting the surface plasmon polariton (SPP) mode on the gold film surface. At a specific wavelength, the core mode of the V-DC-PCF and SPP mode have the same propagation constant, so the mode coupling occurs due to the phase-matching condition. The two air holes in the first layer along the X-direction of the V-DC-PCF are missing to form the two cores, which are labeled as the cores A and B, respectively. In the cladding region of the V-DC-PCF, there are two other sizes of air holes. The diameter of the smaller air holes on the left and right sides is d_2, and the diameter of the larger air holes on the upper and lower sides is d_3. In practice, such a V-DC-PCF can be fabricated with the stack-and-draw method, and the gold film can be selectively coated on the most central air hole by the chemical vapor deposition or magnetron sputtering technique [33,40,47].
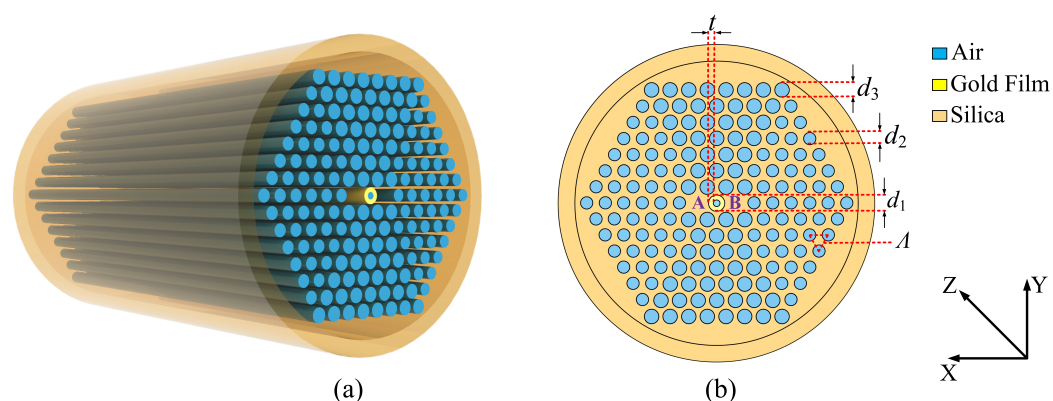
Figure 1. The three-dimensional (**a**) and cross-sectional (**b**) structures of the proposed V-shape dual-core photonic crystal fiber (V-DC-PCF) polarization beam splitter (PBS).

The material dispersion of the silica can be obtained by the Sellmeier equation as [49]

$$n^2(\lambda) = 1 + \frac{A_1\lambda^2}{\lambda^2 - B_1^2} + \frac{A_2\lambda^2}{\lambda^2 - B_2^2} + \frac{A_3\lambda^2}{\lambda^2 - B_3^2} \tag{1}$$

where λ is the wavelength of free space. The related parameters of the Sellmeier equation for the silica material are shown in Table 1.

Table 1. The related parameters of the Sellmeier equation for the silica material.

A_1	A_2	A_3	$B_1(\mu m)$	$B_2(\mu m)$	$B_3(\mu m)$
0.6961663	0.4079426	0.8974794	0.0684043	0.1162414	9.896161

The relative dielectric constant of the gold material can be described by the Drude-Lorentz model [50]

$$\varepsilon_m = \varepsilon_\infty - \frac{\omega_D^2}{\omega(\omega - j\gamma_D)} - \frac{\Delta\varepsilon \cdot \Omega_L^2}{(\omega^2 - \Omega_L^2) - j\Gamma_L\omega} \tag{2}$$

where ω is the angle frequency of the guided-wave, ε_∞ and $\Delta\varepsilon$ are the high frequency dielectric constant and weighted coefficient, ω_D and γ_D are the plasma and damping frequencies, and Ω_L and Γ_L are the frequency and bandwidth of the Lorentz oscillator, respectively. The specific parameters of the Drude-Lorentz model for the gold material are shown in Table 2.

Table 2. The specific parameters of the Drude-Lorentz model for the gold material.

ε_∞	$\Delta\varepsilon$	$\omega_D/2\pi(THz)$	$\gamma_D/2\pi(THz)$	$\Omega_L/2\pi(THz)$	$\Gamma_L/2\pi(THz)$
5.9673	1.09	2113.6	15.92	650.07	104.86

The *CLs* in the X-pol and Y-pol directions of the V-DC-PCF PBS can be described as [51]

$$CL_X = \frac{\lambda}{2\left|(n_{even}^X - n_{odd}^X)\right|} \tag{3}$$

$$CL_Y = \frac{\lambda}{2\left|(n_{even}^Y - n_{odd}^Y)\right|} \tag{4}$$

where CL_X and CL_Y represent the CL of the X-pol and Y-pol, respectively, λ is the wavelength of the initial incident light, and n_{even}^X, n_{odd}^X, n_{even}^Y, and n_{odd}^Y represent the effective refractive indices (ERIs) of the even and odd modes in the X-pol and Y-pol, respectively.

The CLR can be calculated by [52]

$$CLR = \frac{CL_Y}{CL_X} \tag{5}$$

When the CLR = 2 or 1/2, the optimal SL can be obtained.

For the proposed V-DC-PCF PBS, we only need to consider the case that the initial incident light enters the core A or B since the geometric structure of the cores A and B are identical and symmetrical. In this work, when supposing that the initial incident light entering the core A, the output powers P_out of the X-pol and Y-pol in the core A can be described as [53]

$$P_{\text{out,A}}^{X,Y} = P_{in}\cos^2\left(\frac{\pi}{2}\frac{PL}{CL_{X,Y}}\right) \tag{6}$$

where P_in is the power of the initial incident light, and PL is the propagation length inside the V-DC-PCF PBS.

The ER of the core A, which is considered as a significant parameter for evaluating the splitting performance of the V-DC-PCF PBS, can be calculated by [54]

$$ER_A = 10\log_{10}\frac{P_{out,A}^X}{P_{out,A}^Y} \tag{7}$$

The IL of the X-pol and Y-pol in the core A of the V-DC-PCF PBS can be described as [55]

$$IL_{X,Y} = -10\log_{10}\frac{P_{out,A}^{X,Y}}{P_{in}} \tag{8}$$

3. Simulation Results and Discussion

The finite element method is used to investigate the propagation characteristics of the proposed V-DC-PCF [56,57]. The initial fiber structure parameters are set as following: d_1 = 0.95 μm, d_2 = 1.20 μm, d_3 = 1.40 μm, Λ = 2.20 μm, and t = 55 nm. In the simulation, the material coefficients including the refractive indices of the silica and air and the relative dielectric constant of the gold material are set after the simulation model is established. Then, a perfect matching layer (PML), whose thickness is 10 μm and refractive index is n_silica+0.03, is added to the outermost edge of the gold film-coated V-DC-PCF so as to absorb the radiation energy [58]. Moreover, the grid sizes of the silica, air holes, and PML are set as $\lambda/4$, and the grid size of the most central air hole coated with gold film is set as $\lambda/6$.

When the V-DC-PCF is coated without gold film and with gold film, the ERIs of the X-pol and Y-pol even and odd modes and second-order SPP mode are shown in Figure 2a,b, respectively. It can be seen from Figure 2a,b that for the V-DC-PCF without gold film, the ERIs of the X-pol and Y-pol even and odd modes decrease approximately linearly with the increase of wavelength. Moreover, the ERIs of the X-pol and Y-pol odd modes decrease more obviously than that of the X-pol and Y-pol even modes at the longer wavelength side, but the differences between the X-pol or Y-pol even and odd modes are very small. According to Equations (3) and (4), we can infer that the CL_X and CL_Y will also change in the approximately linear trend and have large values. In contrast, when the V-DC-PCF is coated with gold film, the ERIs of the X-pol and Y-pol even modes still decrease approximately linearly as the wavelength increases. However, there are two cross points between the ERIs of the X-pol and Y-pol odd modes and second-order SPP mode at wavelengths 1.178 and 1.159 μm, respectively, where the phase-matching condition is satisfied. According to the coupled mode theory, the X-pol and Y-pol odd modes occur to

couple with the second-order SPP mode at wavelengths 1.178 and 1.159 μm, respectively. In addition, it can be seen from Figure 2a,b that before the phase-matching wavelengths, the ERIs of the X-pol and Y-pol odd modes decrease rapidly, along with a relatively small and stable slope. Hence, the differences between the ERIs of the X-pol and Y-pol even and odd modes increase rapidly with the increase of wavelength. The ERIs of the X-pol and Y-pol odd modes increase significantly at wavelengths 1.178 and 1.159 μm, respectively, and there are maximum differences between the ERIs of the X-pol and Y-pol even and odd modes. Thus, the CL_X and CL_Y will have significant changes at wavelengths 1.178 and 1.159 μm, respectively. But after the phase-matching wavelengths, the ERIs of the X-pol and Y-pol odd modes first decrease rapidly and then maintain a relatively stable slope. Finally, the relatively stable slope of the ERIs of the X-pol and Y-pol odd modes will be smaller than that of the ERIs of the X-pol and Y-pol even modes as the wavelength increases. Therefore, the differences between the ERIs of the X-pol and Y-pol even and odd modes first decrease and then increase as the wavelength increases. Figure 3a,b show the mode field distributions of the X-pol and Y-pol even and odd modes and second-order SPP mode calculated at wavelengths 1.178 and 1.159 μm, respectively. From Figure 3a,b, the mode field distributions of the X-pol and Y-pol even modes have no change at wavelengths 1.178 and 1.159 μm, respectively. But the mode field energies of the X-pol and Y-pol odd modes and second-order SPP mode occur to transfer at the two wavelengths. It further confirms the previous conclusion that only the X-pol and Y-pol odd modes and second-order SPP mode occur to couple at the phase-matching wavelengths.
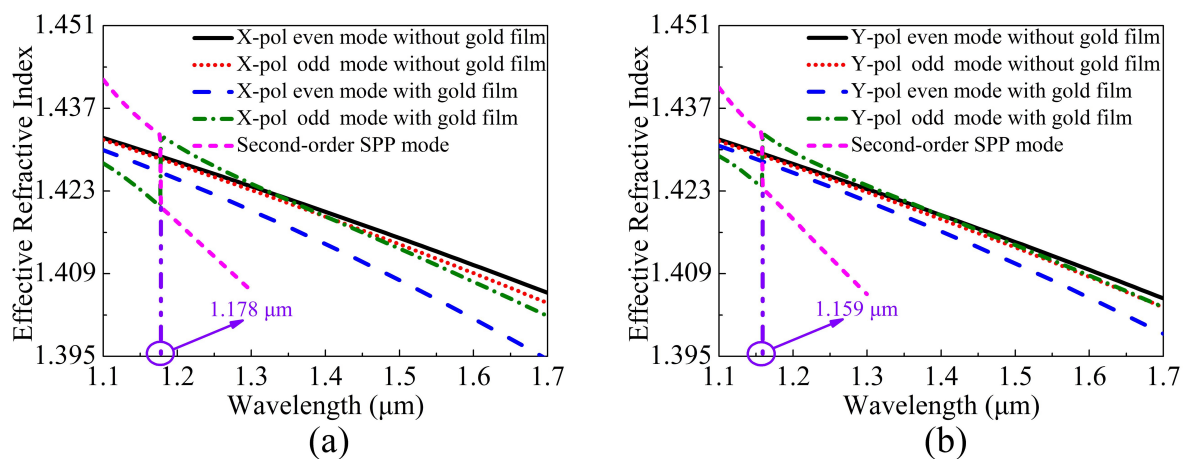

Figure 2. The ERIs of the (**a**) X-pol and (**b**) Y-pol even and odd modes and second-order surface plasmon polariton (SPP) mode calculated as functions of wavelength when the V-DC-PCF is coated without gold film and with gold film, respectively.

The relationships between the CL_X, CL_Y, and *CLR* and wavelength are shown in Figure 4a,b, respectively, when the V-DC-PCF is coated without gold film and with gold film. It can be seen from Figure 4a that when the V-DC-PCF is coated without gold film, the CL_X and CL_Y decrease gradually, and the corresponding *CLR* also decreases in an approximately linear trend as the wavelength increases. According to Equations (3) and (4) and the above analysis, when the V-DC-PCF is coated with gold film, the CL_X and CL_Y decrease rapidly before the phase-matching wavelengths, and occur to change significantly at wavelengths 1.178 and 1.159 μm, respectively, as shown in Figure 4b. After the phase-matching wavelengths, the CL_X and CL_Y increase first and then decrease. At this time, according to Equation (5), the *CLR* decreases rapidly before wavelength 1.159 μm, has a significant change between wavelength 1.159 and 1.178 μm, and increases first and then decreases after wavelength 1.178 μm. However, after wavelength 1.178 μm, the overall change of the *CLR* is relatively flat. In addition, the *CLR* has the two intersections, where the *CLR* is equal to 1.7. By comparing Figure 4a,b, the maximum *CL* for the V-DC-PCF with gold film is smaller than the minimum *CL* for the V-DC-PCF without gold film, which

has a direct effect on the *SL* of the V-DC-PCF PBS. From the above analysis, it is possible to achieve a PBS with the shorter *SL* and larger *SB* by using a V-DC-PCF with gold film.
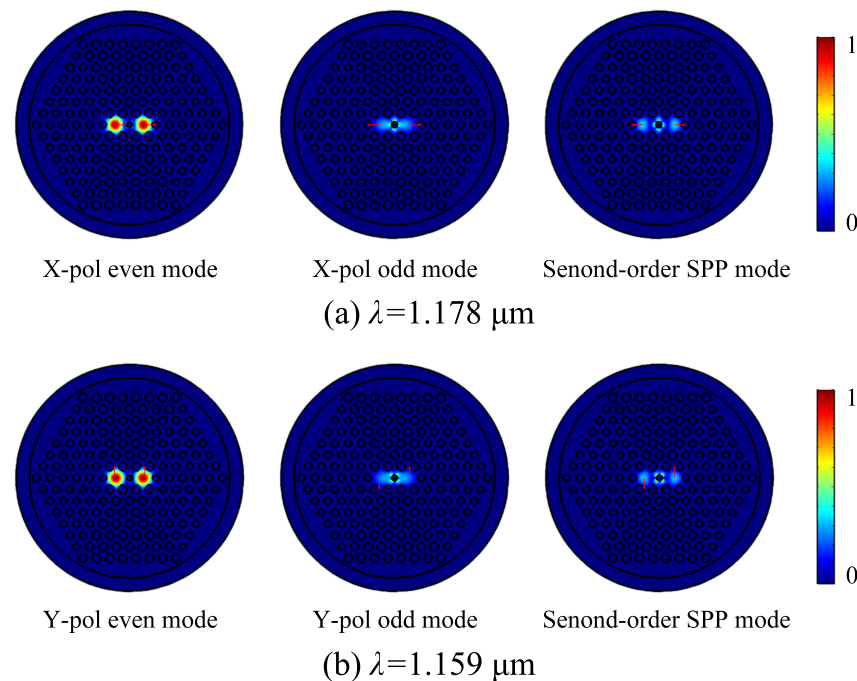

(a) λ=1.178 µm

(b) λ=1.159 µm

Figure 3. The mode field distributions of the (**a**) X-pol and (**b**) Y-pol even and odd modes and second-order SPP mode of the V-DC-PCF calculated at wavelengths 1.178 and 1.159 µm, respectively.
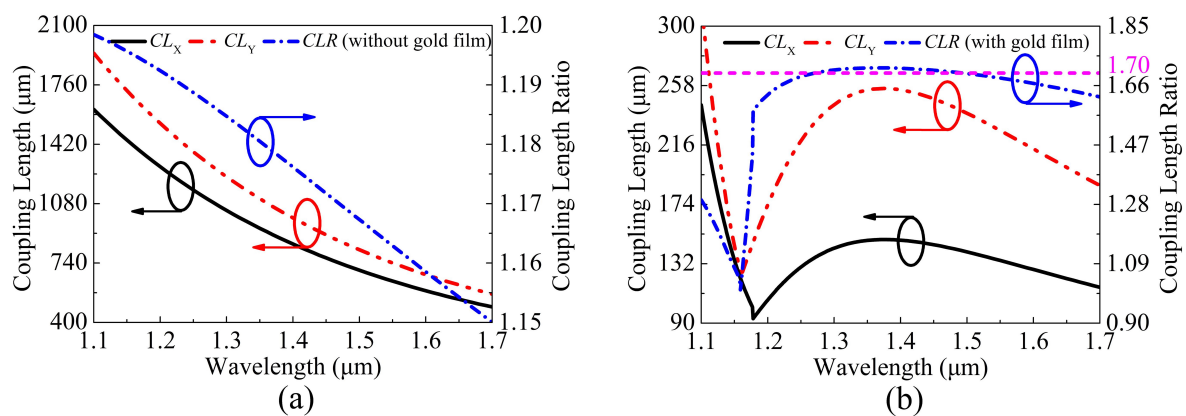

Figure 4. The CL_X, CL_Y, and *CLR* as functions of the wavelength when the V-DC-PCF is coated (**a**) without gold film and (**b**) with gold film.

The structure parameters of the proposed V-DC-PCF PBS with gold film need to be optimized to satisfy the condition of *CLR* = 2, which corresponds to the optimal *SL*. When the fiber structure parameters, including d_1, d_2, d_3, Λ, and t are changed, respectively, the ERIs of the X-pol and Y-pol even and odd modes will occur to change in different degrees, which can also cause the changes of the CL_X, CL_Y, and *CLR*. The variations of the CL_X, CL_Y, and *CLR* of the proposed V-DC-PCF PBS are shown in Figure 5a,b when d_1 is chosen as 0.90, 0.95, and 1.00 µm, respectively. It can be seen from Figure 5a that the CL_X and CL_Y decrease as d_1 increases at the short wavelength side. At the long wavelength side, as d_1 increases, the CL_X still decreases slightly, while the CL_Y shows a slightly increased trend. The *CLR* gradually increases as d_1 increases, and the phase-matching wavelength occurs to red-shift, as shown in Figure 5b.
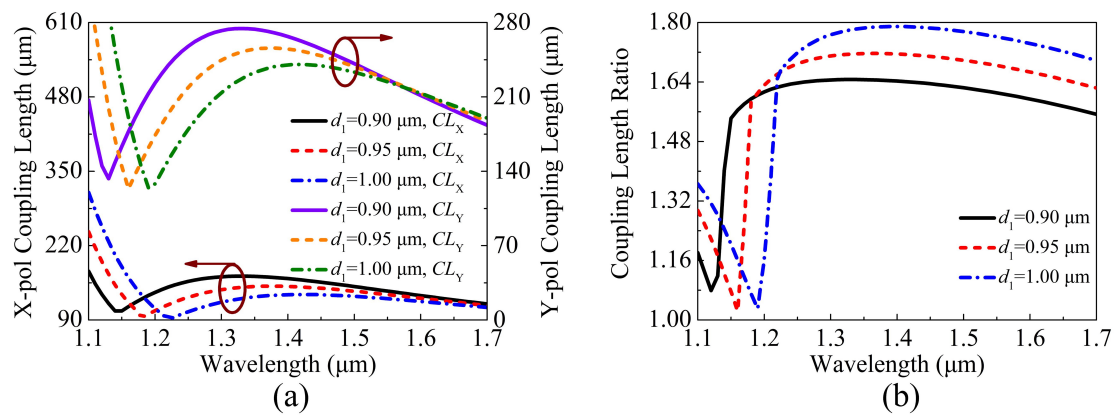
Figure 5. The variations of the (**a**) CL_X, CL_Y, and (**b**) CLR of the proposed V-DC-PCF PBS for different d_1.

The variations of the CL_X, CL_Y, and CLR of the proposed V-DC-PCF PBS are shown in Figure 6a,b when d_2 is chosen as 1.00, 1.20, and 1.40 µm, respectively. It can be seen from Figure 6a,b that as d_2 increases, the CL_X and CL_Y gradually decrease while the CLR shows an increased trend. In addition, the change of the phase-matching wavelength is not obvious, and only a slight red-shift occurs as d_2 increases.
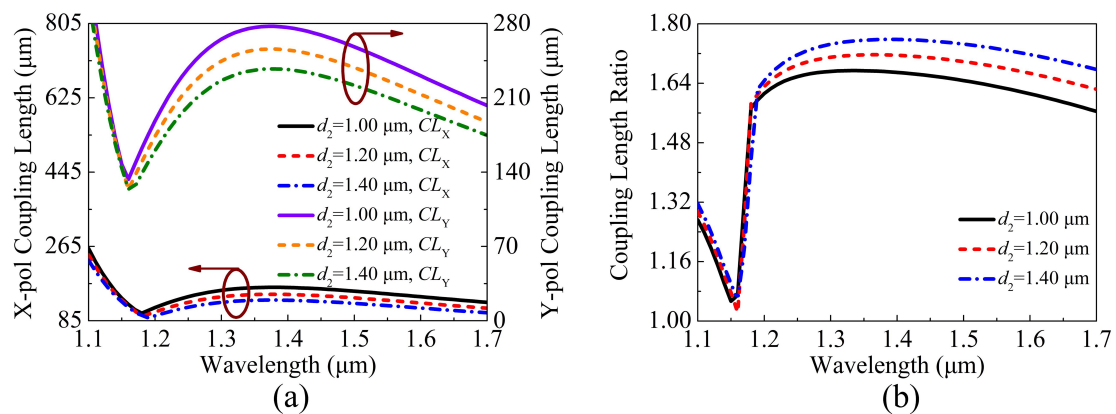

Figure 6. The variations of the (**a**) CL_X, CL_Y, and (**b**) CLR of the proposed V-DC-PCF PBS for different d_2.

When d_3 is chosen as 1.20, 1.40, and 1.60 µm, respectively, the variations of the CL_X, CL_Y, and CLR of the proposed V-DC-PCF PBS are shown in Figure 7a,b. From Figure 7a, as d_3 increases, the CL_X decreases slightly at the short wavelength side and remains nearly unchanged at the long wavelength side. In comparison, the CL_Y gradually increases as d_3 increases, and the corresponding change amplitude at the long wavelength side is larger than that at the short wavelength side. As shown in Figure 7b, as d_3 increases, the CLR gradually increases, and the position of the phase-matching wavelength remains unchanged.

The variations of the CL_X, CL_Y and CLR of the proposed V-DC-PCF PBS are shown in Figure 8a,b when Λ is chosen as 2.1, 2.2, and 2.3 µm, respectively. Figure 8a,b, as Λ increases, the CL_X and CL_Y gradually increase, but the CLR shows a decreasing trend. In addition, the change of the phase-matching wavelength is not obvious, along with a small shift towards the short wavelength side. By comparing the results shown in Figures 5b, 6b, 7b, and 8b, it is found that the change of Λ has the most remarkable influence on the CLR.
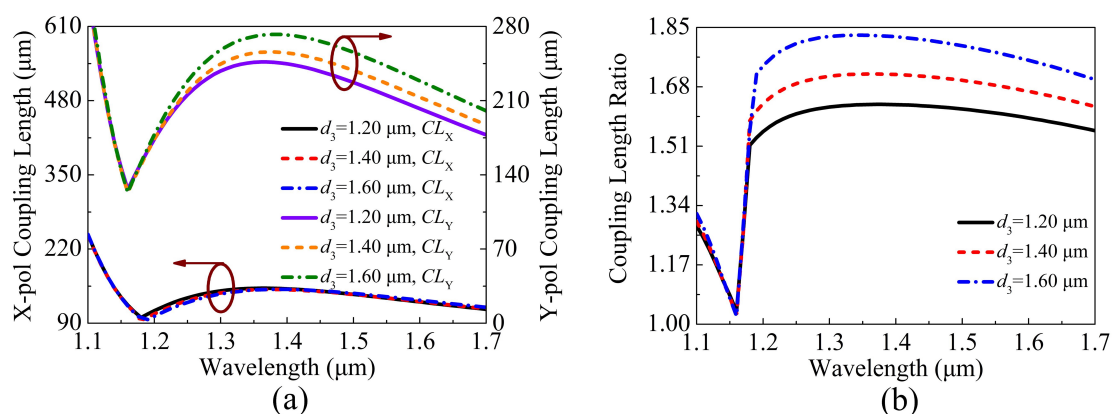
Figure 7. The variations of the (**a**) CL_X, CL_Y, and (**b**) CLR of the proposed V-DC-PCF PBS for different d_3.

Figure 9a,b show the variations of the CL_X, CL_Y, and CLR of the proposed V-DC-PCF PBS when t is chosen as 45, 55, and 65 nm, respectively. It can be seen from Figure 9a that as t increases, the CL_X and CL_Y increase at the short wavelength side and decrease at the long wavelength side. It can be seen from Figure 9b that as t increases, the CLR increases at the short wavelength side and decreases at the long wavelength side, and the position of the phase-matching wavelength gradually shifts towards the short wavelength side.
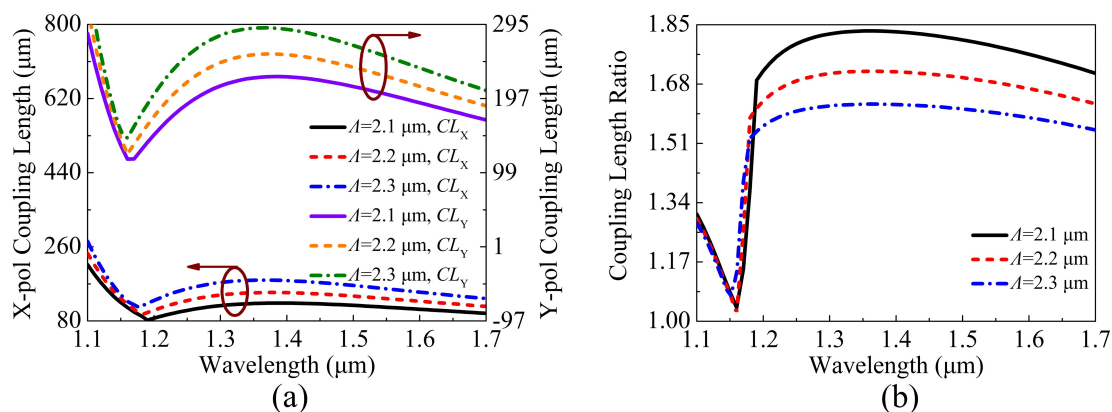

Figure 8. The variations of the (**a**) CL_X, CL_Y, and (**b**) CLR of the proposed V-DC-PCF PBS for different Λ.
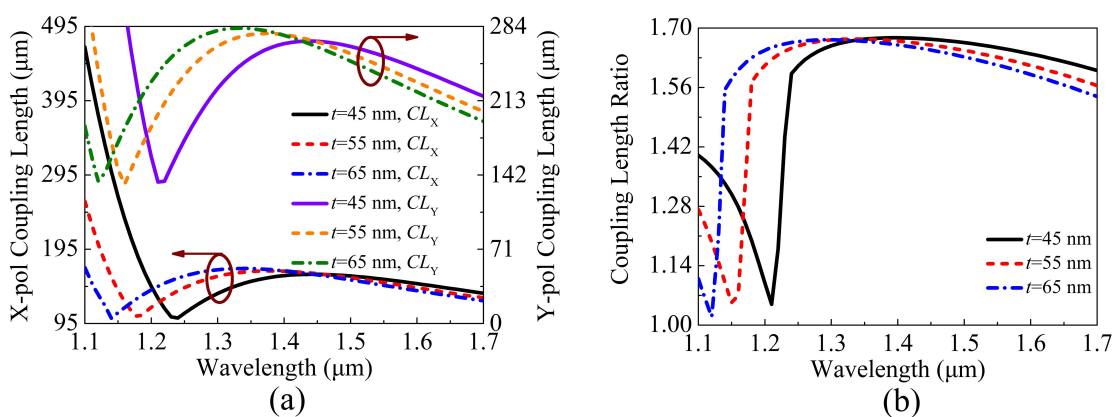

Figure 9. The variations of the (**a**) CL_X, CL_Y, and (**b**) CLR of the proposed V-DC-PCF PBS for different t.

Based on the above analysis, the influence rule of the structure parameters of the proposed V-DC-PCF PBS on the CL_X, CL_Y, and CLR can be clearly known. Thus, the empirical steps for designing such a V-DC-PCF PBS can be summarized as following. First,

by together adjusting d_1 and t, the phase-matching condition can be achieved at the shorter wavelength, and the value of the *CLR* is close to 2. At this time, a relatively flat *CLR* curve can be obtained in the desired band. Second, by together adjusting d_2, d_3, and Λ, the *CLR* curve with the relatively flat profile and the value of 2 can be obtained when the phase-matching wavelength does not change obviously. Thus, the optimized structure parameters of the proposed V-DC-PCF PBS are chosen as follows: d_1 = 1.00 μm, d_2 = 1.41 μm, d_3 = 1.50 μm, Λ = 2.10 μm, and t = 46.5 nm. At this time, the variations of the optimal CL_X, CL_Y, and *CLR* of the proposed V-DC-PCF PBS and the corresponding zoomed flat region of the *CLR* are shown in Figure 10a,b, respectively. From Figure 10a, the CL_X and CL_Y have significant changes at the phase-matching wavelengths 1.277 and 1.243 μm, respectively. Moreover, the *CLR* is approximately equal to 2 in a wide wavelength range of above 1.277 μm. From Figure 10b, the value of the *CLR* changes from 1.974 to 2.051 in the wavelength range from 1.32 to 1.68 μm, and the maximum difference of the *CLR* between wavelength 1.32 and 1.68 μm is 0.077. In addition, the values of the *CLR* at wavelengths 1.610, 1.631, and 1.650 μm are 2.01, 2.00, and 1.99, respectively, which are approximately equal to 2. It is worth noting that although the value of the *CLR* is also equal to 1.99, 2.00, and 2.01 at other three shorter wavelengths, but the corresponding slope variation of the *CLR* is larger, which will affect the overall bandwidth to a great extent.
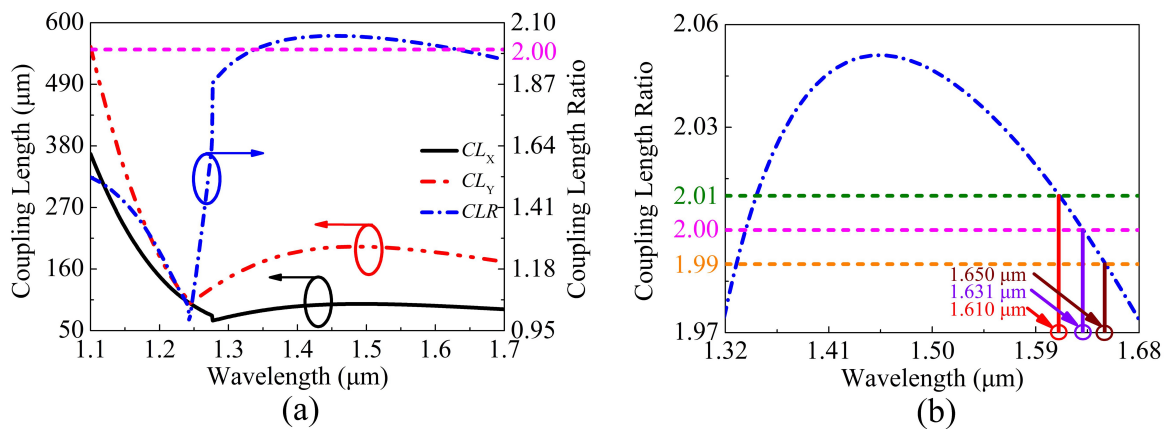

Figure 10. The optimal CL_X, CL_Y, and *CLR* of the proposed V-DC-PCF PBS, and (**b**) the zoomed flat region of the *CLR*.

In the following, the relationships between the output powers P_{out} of the X-pol and Y-pol of the proposed V-DC-PCF PBS and *PL* at the three wavelengths 1.610, 1.631, and 1.650 μm are shown in Figure 11a–c, respectively. From Figure 11a–c, P_{out} of the X-pol reaches the maximum values when the *PL* is located at 188, 185, and 182 μm, respectively. In contrast, the corresponding P_{out} of the Y-pol reaches 0 when the *PL* is located at 188, 185, and 182 μm, respectively. This phenomenon indicates that the X-pol light only exists in the core A while the Y-pol light only exists in the core B at the three *PLs*. Therefore, the *SL* of the proposed V-DC-PCF PBS may be 182, 185, or 188 μm. Moreover, another notable phenomenon is that the total P_{out} decreases slightly as the *PL* increases. This is mainly because a fraction of the energy always propagates on the surface of the gold film, leading to the increase of the ohmic loss.

When the *SL* is equal to 182, 185, and 188 μm, respectively, the relationships between the *ERs* in the core A of the proposed V-DC-PCF PBS and wavelength are shown in Figure 12. It can be seen from Figure 12 that for the *SLs* of 182 and 185 μm, the *ERs* are less than 20 dB in some wavelength ranges. In contrast, when *SL* is equal to 188 μm, the *ER* is always larger than 20 dB in a wide wavelength range from 1.359 to 1.677 μm. Figure 13 shows the relationships between the *ILs* of the X-pol and Y-pol in the core A of the proposed V-DC-PCF PBS and wavelength when the *SL* is equal to 182, 185, and 188 μm, respectively. From Figure 13, for the *SLs* of 182, 185, and 188 μm, the maximum *IL* of the X-pol and Y-pol is 0.22 dB in the wavelength range of 1.359 to 1.677 μm. Such a small

IL can meet the actual application requirements. Because the proposed V-DC-PCF PBS has the ultra-short *SL*, the bending loss can be neglected. Therefore, we can draw a conclusion that for the proposed V-DC-PCF PBS, the optimal *SL* is 188 μm, the *SB* covers the entire E + S + C + L + U band, and the *ILs* of the X-pol and Y-pol are less than 0.22 dB.

The comparisons between the proposed V-DC-PCF PBS and reported SPR-based DC-PCF PBS are shown in Table 3. From Table 3, only the *SB* of the SPR-based DC-PCF PBS reported in Ref [12] is larger than that of the proposed V-DC-PCF PBS. However, in Ref [12], the *SL* and minimum *IL* are 4.036 mm and 0.8 dB, respectively, while they are only 188 μm and 0.22 dB in this work. Moreover, the air holes of the DC-PCF PBS reported in Ref [12] are arranged in a square lattice, so it is difficult to fabricate. In addition, only the *SL* of the SPR-based DC-PCF PBS reported in Ref [25] is shorter than that of this work. However, in Ref [25], the *SB*, which covers the S + C + L band, is much narrower than that of this work, and the *IL* is not given. Moreover, the air holes of square lattice of the DC-PCF PBS reported in Ref [25] also increase the difficulty of fabrication. In summary, the proposed V-DC-PCF PBS has the good comprehensive performances.
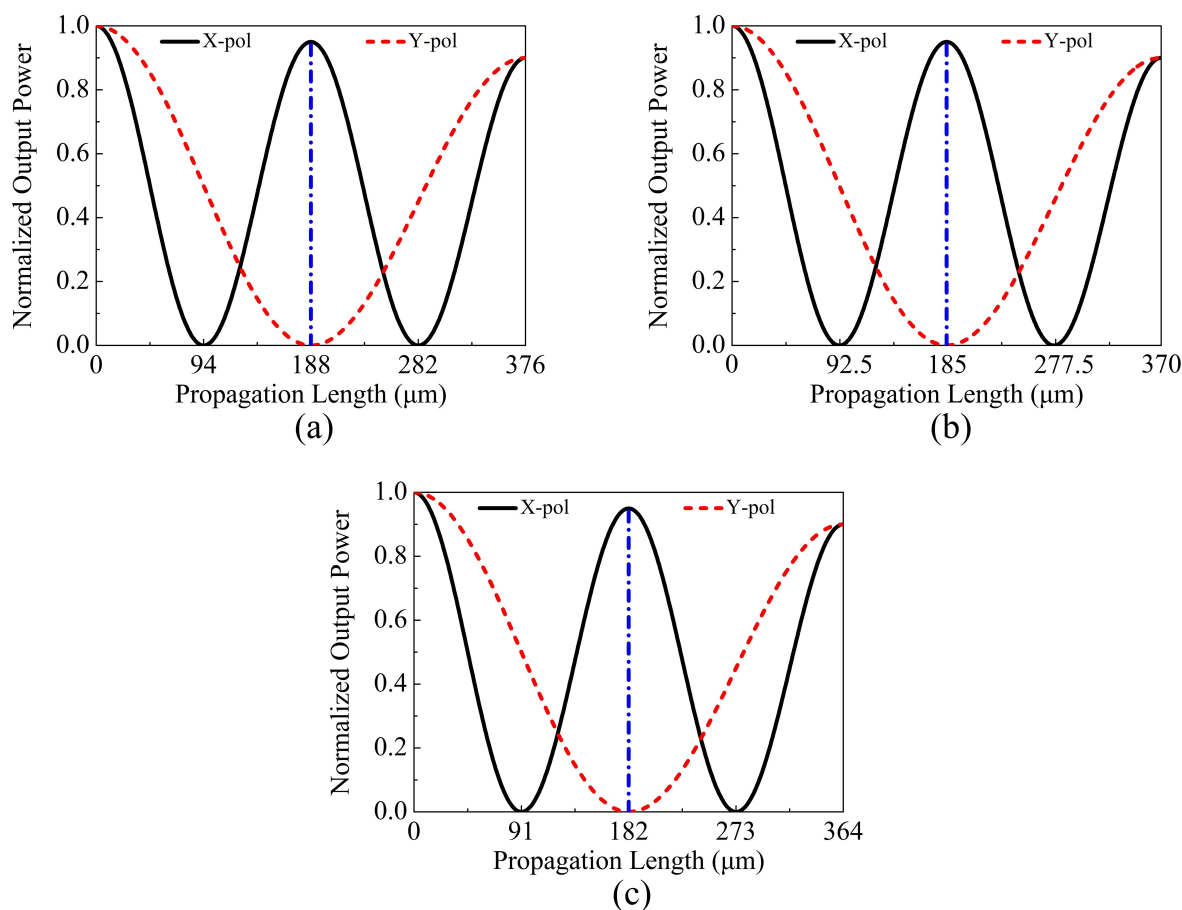

Figure 11. The relationships between the output powers P_{out} of the X and Y-pol of the proposed V-DC-PCF PBS and *PL* at the three wavelengths (**a**) 1.610, (**b**) 1.631, and (**c**) 1.650 μm, respectively.
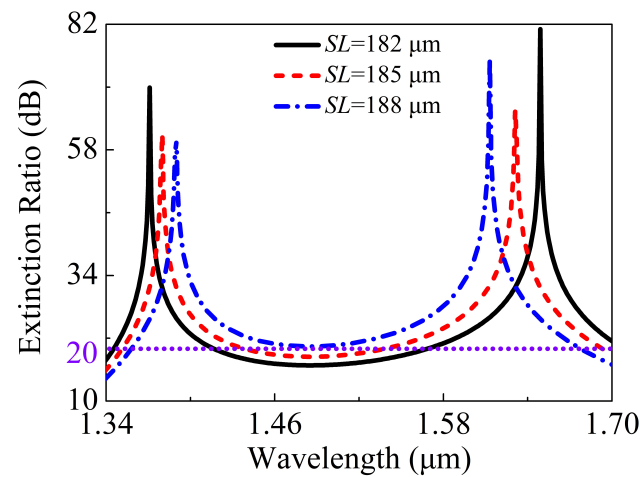
Figure 12. The *ERs* in the core A of the proposed V-DC-PCF PBS as functions of the wavelength for different *SL*.

Table 3. Comparisons between the proposed V-DC-PCF PBS and reported surface plasmon resonance (SPR)-based DC-PCF PBS.

Ref.	DC-PCF Structure	Gold Film or Wire	*SB*	*SL*	Max *IL*
[12]	Square lattice with circular air holes	Gold wire	O + E + S + C + L + U band	4.036 mm	0.8 dB
[13]	Hexagonal lattice with elliptical air holes	Gold wire	S + C + L + U band	254.6 μm	N/A
[14]	Hexagonal lattice with circular air holes	Gold wire	O and C bands	830 μm	N/A
[15]	D-shape hexagonal lattice with circular air holes	Gold film	C band	0.782 mm	1.5 dB
[16]	Hexagonal lattice with circular air holes	Gold wire	S + C + L + U band	577.5 μm	N/A
[17]	Rectangle lattice with circular air holes	Two gold wires	E + C band	1 mm	N/A
[18]	Hexagonal lattice with circular air holes	Gold film	S + C + L band	5.112 mm	N/A
[24]	Hexagonal lattice with circular air holes	Elliptical gold wire	C band	1.079 mm	N/A
[25]	Square lattice with circular air holes	Gold film	S + C + L band	47.26 μm	N/A
This work	Hexagonal lattice with circular air holes	Gold film	E + S + C + L + U band	188 μm	<0.22 dB

The *ERs* in the core A and *ILs* of the X-pol and Y-pol in the core A of the proposed V-DC-PCF PBS are shown in Figure 14a,b when *t* changes ±1%. From Figure 14a, the wavelength range of the *ER* larger than 20 dB changes slightly, which indicates that the proposed V-DC-PCF PBS still has a wide *SB*. From Figure 14b, the *ILs* of the X-pol and Y-pol are always less than 0.22 dB in each *SB*. Thus, *t* has good error-tolerant rate in the actual coating process.
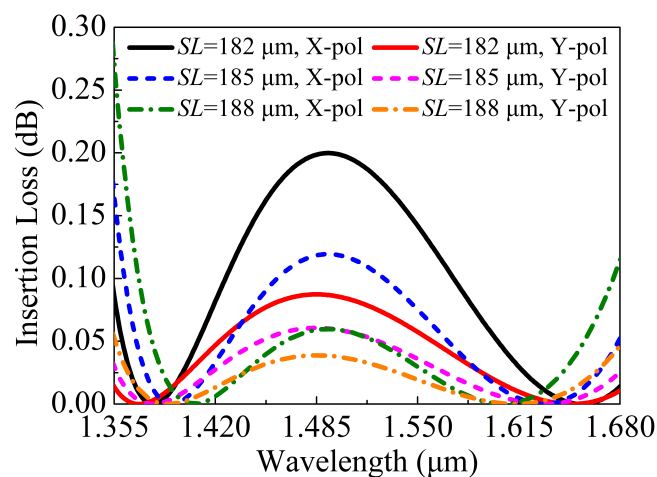
Figure 13. The *ILs* of the X-pol and Y-pol in the core A of the proposed V-DC-PCF PBS as functions of the wavelength for different *SL*.
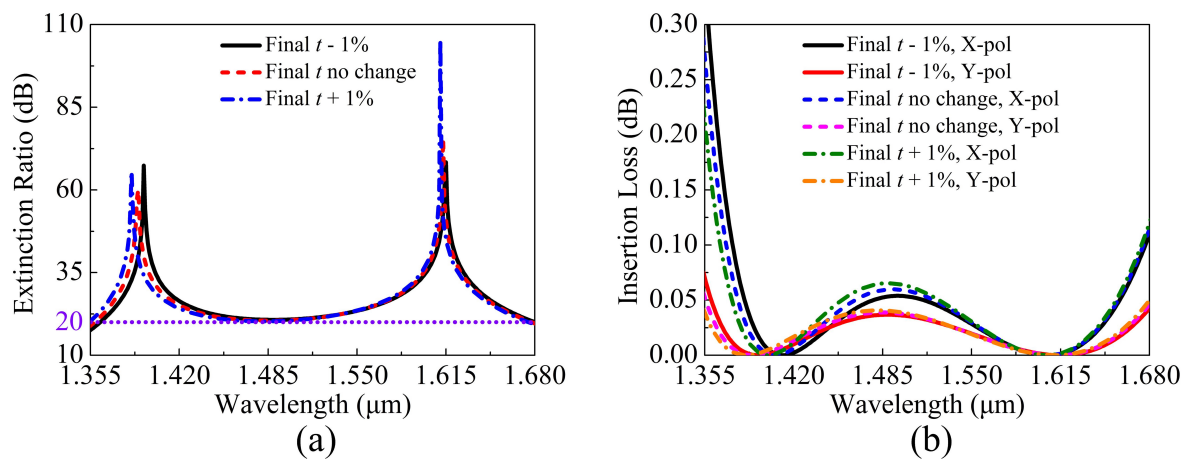

Figure 14. (**a**) *ERs* in the core A and (**b**) *ILs* of the X-pol and Y-pol in the core A of the proposed V-DC-PCF PBS as functions of wavelength when *t* has the distortion of ±1%.

4. Conclusions

In summary, a novel gold film-coated V-DC-PCF PBS based on the SPR effect is proposed. The CL_X, CL_Y, and CLR of the proposed V-DC-PCF PBS coated without gold film and with gold film are investigated. The empirical steps for designing such a V-DC-PCF PBS are summarized by analyzing the effects of the fiber structure parameters on the CL_X, CL_Y, and CLR. The CLR of 2 can be obtained at the three wavelengths 1.610, 1.631, and 1.650 μm. When the *SLs* are equal to 188, 185, and 182 μm, the relationships between the *ER*, *IL* and wavelength are investigated, respectively. The proposed V-DC-PCF PBS has the good comprehensive performances, including the *SL* of 188 μm, *IL* of less than 0.22 dB, and *SB* of covering the E + S + C + L + U band. It is believed that the proposed V-DC-PCF PBS can find important applications in the laser, sensing, and dense wavelength division multiplexing systems.

Author Contributions: Y.Q.: Conceptualization, Formal analysis, Writing-original draft, Methodology and Investigation. J.Y.: Supervision, Formal analysis, Methodology, Writing-review and editing. S.Q.: Supervision, Formal analysis, Writing-review and editing. X.Z.: Supervision, Formal analysis, Writing-review and editing. F.L.: Formal analysis, Writing-review and editing. B.Y.: Formal analysis, Writing-review and editing. Q.W.: Supervision, Formal analysis, Methodology, Writing-review and editing. K.W.: Formal analysis, Writing-review and editing. X.S.: Supervision, Writing-review and editing. K.L.: Supervision, Writing-review and editing. C.Y.: Supervision, Writing-review and editing. All authors have read and agreed to the published version of the manuscript.

Conflicts of Interest: The authors declare no conflict of interest.

References

1. Knight, J.C.; Birks, T.A.; Russell, P.S.J.; Atkin, D.M. All-silica single-mode optical fiber with photonic crystal cladding. *Opt. Lett.* **1996**, *21*, 1547–1549. [CrossRef]
2. Liu, Q.; Ma, Z.; Wu, Q.; Wang, W.L. The biochemical sensor based on liquid-core photonic crystal fiber filled with gold, silver and aluminum. *Opt. Laser Technol.* **2020**, *130*, 106363. [CrossRef]
3. Úsuga-Restrepo, J.E.; Guimarães, W.M.; Franco, M.A.R. All-fiber circular polarization beam splitter based on helically twisted twincore photonic crystal fiber coupler. *Opt. Laser Technol.* **2020**, *58*, 102285.
4. Feng, X.X.; Du, H.J.; Li, S.G.; Zhang, Y.N.; Liu, Q.; Gao, X.Y. A polarization filter based on photonic crystal fiber with asymmetry around gold-coated holes. *Plasmonics* **2018**, *13*, 1271–1275. [CrossRef]
5. Yu, R.W.; Chen, Y.X.; Shui, L.L.; Xiao, L.M. Hollow-core photonic crystal fiber gas sensing. *Sensors* **2020**, *20*, 2996. [CrossRef]
6. Yao, C.Y.; Xiao, L.M.; Gao, S.F.; Wang, Y.Y.; Wang, P.; Kand, R.F.; Jine, W.; Rena, W. Sub-ppm CO detection in a sub-meter-long hollow-core negative curvature fiber using absorption spectroscopy at 2.3 μm. *Sens. Actuat. B Chem.* **2020**, *303*, 127238. [CrossRef]
7. Wang, J.; Pei, L.; Wang, J.S.; Ruan, Z.L.; Zheng, J.J.; Li, J.; Ning, T.G. Magnetic field and temperature dual-parameter sensor based on magnetic fluid materials filled photonic crystal fiber. *Opt. Express* **2020**, *28*, 1456–1471. [CrossRef]
8. Shakya, A.K.; Singh, S. Design of dual polarized tetra core PCF based plasmonic RI sensor for visible-IR spectrum. *Opt. Commun.* **2021**, *478*, 126372. [CrossRef]
9. Chu, L.H.; Liu, M.; Shum, P.; Fu, Y.B. Simultaneous achievement of an ultrashort length and a high extinction ratio polarization splitter based on the dual-core photonic crystal fiber with $Ge_{20}Sb_{15}Se_{65}$ glass. *Appl. Opt.* **2019**, *58*, 7892–7896. [CrossRef]
10. Rahman, M.M.; Khaleque, A.; Rahman, M.T.; Rabbi, F. Gold-coated photonic crystal fiber based polarization filter for dual communication windows. *Opt. Commun.* **2020**, *461*, 125293. [CrossRef]
11. Reyes-Vera, E.; Úsuga-Restrepo, J.; Gomez, F.; Gómez-Cardona, N. Novel multiband polarization beam splitter based on a dual-core transversally chirped microstructured optical fiber. *Third Int. Conf. Appl. Opt. Photonics* **2017**, *10453*, 1045334.
12. Jiang, L.H.; Zheng, Y.; Hou, L.T.; Zheng, K.; Peng, J.Y.; Zhao, X.T. An ultrabroadband polarization splitter based on square-lattice dualcore photonic crystal fiber with a gold wire. *Opt. Commun.* **2015**, *351*, 50–56. [CrossRef]
13. Khaleque, A.; Hattori, H.T. Ultra-broadband and compact polarization splitter based on gold filled dual-core photonic crystal fiber. *J. Appl. Phys.* **2015**, *118*, 143101. [CrossRef]
14. Jimenez-Durango, C.; Reyes-Vera, E.; Gomez-Cardona, N. Ultra-short polarization beam splitter to operate in two communication bands based on a gold-filled dual-core photonic crystal fiber. In *Latin America Optics and Photonics Conference*; OSA Technical Digest (Optical Society of America): Washington, DC, USA, 2018.
15. Chen, H.L.; Li, S.G.; An, G.W.; Li, J.S.; Fan, Z.K.; Han, Y. Polarization splitter based on d-shaped dual-core photonic crystal fibers with gold film. *Plasmonics* **2015**, *10*, 57–61. [CrossRef]
16. Sun, B.; Chen, M.Y.; Zhang, Y.K.; Zhou, J. Polarization-dependent coupling characteristics of metal-wire filled dual-core photonic crystal fiber. *Opt. Quant. Electron.* **2015**, *47*, 441–451. [CrossRef]
17. An, G.W.; Li, S.G.; Yan, X.; Yuan, Z.Y.; Zhang, X.N. High-birefringence photonic crystal fiber polarization filter based on surface plasmon resonance. *Appl. Opt.* **2016**, *55*, 1262–1266. [CrossRef]
18. Wang, X.Y.; Yan, X.; Li, S.G.; Zhang, X.N. Tunable surface plasmon resonance polarization beam splitter based on dual-core photonic crystal fiber with magnetic fluid. *Opt. Quant. Electron.* **2017**, *49*, 368. [CrossRef]
19. Jiang, H.M.; Wang, E.L.; Zhang, J.; Hu, L.; Mao, Q.P.; Li, Q.; Xie, K. Polarization splitter based on dual-core photonic crystal fiber. *Opt. Express* **2014**, *22*, 30461–30466. [CrossRef]
20. Zi, J.C.; Li, S.G.; An, G.W.; Fan, Z.K. Short-length polarization splitter based on dual-core photonic crystal fiber with hexagonal lattice. *Opt. Commun.* **2016**, *363*, 80–84. [CrossRef]
21. Wang, E.L.; Jiang, H.M.; Xie, K.; Chen, C.; Hu, Z.J. Olarization splitter based on dual core liquid crystal-filled holey fiber. *J. Appl. Phys.* **2016**, *120*, 114501. [CrossRef]
22. He, F.T.; Shi, W.J.; Hui, Z.Q.; Zhan, F.; Zhang, Y.K. A dual-core PCF polarization splitter with five elliptical air holes based on tellurite glass. *Opt. Quant. Electron.* **2017**, *49*, 363. [CrossRef]
23. Wang, J.S.; Pei, L.; Weng, S.J.; Wu, L.Y.; Ning, T.G.; Li, J. Ultrashort polarization beam splitter based on liquid-filled dual-core photonic crystal fiber. *Appl. Opt.* **2018**, *57*, 3847–3852. [CrossRef] [PubMed]
24. Wang, X.Y.; Li, S.G.; Liu, Q.; Fan, Z.K.; Wang, G.Y.; Zhao, Y.Y. High-extinction ratio and short-length polarization splitter based on microstructured optical fiber with tellurite glass. *Opt. Mater.* **2017**, *66*, 542–546. [CrossRef]
25. Lou, J.B.; Cheng, T.L.; Li, S.G. Ultra-short polarization beam splitter with square lattice and gold film based on dual-core photonic crystal fiber. *Optik* **2019**, *179*, 128–134. [CrossRef]

26. Xiao, L.M.; Birks, T.A.; Loh, W.H. Hydrophobic photonic crystal fibers. *Opt. Lett.* **2011**, *36*, 4662–4664. [CrossRef]

27. Zhao, T.T.; Lou, S.Q.; Wang, X.; Zhang, W.; Wang, Y.L. Simultaneous measurement of curvature, strain and temperature using a twin-core photonic crystal fiber-based sensor. *Sensors* **2018**, *18*, 2145. [CrossRef]

28. Wiegandt, F.; Anderson, P.N.; Yu, F.; Treacher, D.J.; Lloyd, D.T.; Mosley, P.J.; Hooler, S.M.; Walmsley, I.A. Quasi-phase-matched high-harmonic generation in gas-filled hollow-core photonic crystal fiber. *Optica* **2019**, *6*, 442–447. [CrossRef]

29. Mridha, M.K.; Novoa, D.; Hosseini, P.; Russel, P.S.J. Thresholdless deep and vacuum ultraviolet Raman frequency conversion in hydrogen-filled photonic crystal fiber. *Optica* **2019**, *6*, 731–734. [CrossRef]

30. Davtyan, S.; Chen, Y.; Frosz, M.H.; Russell, P.S.J.; Novoa, D. Robust excitation and raman conversion of guided vortices in a chiral gas-filled photonic crystal fiber. *Opt. Lett.* **2020**, *45*, 1766–1769. [CrossRef]

31. Fujisawa, T.; Saitoh, K. Geometric-phase-induced arbitrary polarization and orbital angular momentum generation in helically twisted birefringent photonic crystal fiber. *Photonics Res.* **2020**, *8*, 1278–1288. [CrossRef]

32. Ning, D.; Lothar, W.; Markus, A.S.; Nicolai, G.; Russell, P.S.J. High index-contrast all-solid photonic crystal fibers by pressure-assisted melt infiltration of silica matrices. *J. Non-Cryst. Solids* **2010**, *356*, 1829–1836.

33. Knight, J.C.; Broeng, J.; Birks, T.A.; Russell, P.S.J. Photonic band gap guidance in optical fibers. *Science* **1998**, *282*, 1476–1478. [CrossRef] [PubMed]

34. Feng, X.; Mairaj, A.K.; Hewak, D.W.; Monro, T.M. Nonsilica glasses for holey fibers. *J. Lightw. Technol.* **2005**, *23*, 2046–2054. [CrossRef]

35. Li, Y.; Itoh, K.; Watanabe, W.; Yamada, K.; Kuroda, D.; Nishii, J.J.; Jiang, Y.Y. Three-dimensional hole drilling of silica glass from the rear surface with femtosecond laser pulses. *Opt. Lett.* **2001**, *26*, 1912–1914. [CrossRef]

36. Cook, K.; Canning, J.; Leon-saval, S.; Reid, Z.; Hossainmd, A.; Comatt, J.E.; Luo, Y.H.; Peng, G.D. Air-structured optical fiber drawn from a 3D-printed preform. *Opt. Lett.* **2015**, *40*, 3966–3969. [CrossRef]

37. Urich, A.; Maier, R.R.J.; Yu, F.; Knight, J.C.; Hand, D.P.; Shephard, J.D. Silica hollow core microstructured fibres for mid-infrared surgical applications. *J. Non Cryst. Solids* **2013**, *377*, 236–239. [CrossRef]

38. Liang, L.B.; Ju, B.; Long, X.Q.; Liu, J.T.; Rong, S.Y.; Xia, C.M.; Chen, Y.; Hou, Z.Y.; Zhou, G.Y.; Zhao, N. Fabrication and optical properties of Tm^{3+}/Al^{3+} co-doped photonic crystal fiber based on CO_2 laser sintering technology. *J. Abbr.* **2008**, *10*, 142–149. [CrossRef]

39. Chen, Y.; Zhao, N.; Liu, J.T.; Zhu, M.M.; Mai, Y.F.; Zhou, G.Y.; Hou, Z.Y.; Xia, C.M.; Zheng, Y.; Chen, Z.Q. Investigation of photo-darkening effect in ytterbium-doped microstructure optical fiber through the laser sintering fabrication method. *J. Non-Cryst. Solids* **2019**, *521*, 119468. [CrossRef]

40. Sazio, P.J.A.; Correa, A.A.; Finlayson, C.E.; Hayes, J.R.; Scheidemantel, T.J.; Baril, N.F.; Jackson, B.R.; Won, D.J.; Zhang, F.; Margine, E.R.; et al. Microstructured optical fibers as high-pressure microfluidic reactors. *Science* **2006**, *311*, 1583–1586. [CrossRef]

41. Schmidt, M.A.; Sempere, L.N.P.; Tyagi, H.K.; Poulton, C.G.; Russell, P.S.J. Waveguiding and plasmon resonances in two-dimensional photonic lattices of gold and silver nanowires. *Phys. Rev. B* **2008**, *77*, 033417. [CrossRef]

42. Zhan, X.; Wang, R.; Cox, F.M.; Kuhlmey, B.T.; Large, M.C.J. Selective coating of holes in microstructured optical fiber and its application to in-fiber absorptive polarizers. *Opt. Express* **2007**, *15*, 16270–16278. [CrossRef] [PubMed]

43. Lee, H.W.; Schmidt, M.A.; Tyagi, H.K.; Sempere, L.P.; Russel, P.S.J. Polarization dependent coupling to plasmon modes on submicron gold wire in photonic crystal fiber. *Appl. Phys. Lett.* **2008**, *93*, 111102. [CrossRef]

44. Lee, H.W.; Schmidt, M.A.; Russell, R.F.; Joly, N.Y.; Tyagi, H.K.; Uebel, P.; Russel, P.S.J. Pressure-assisted melt-filling and optical characterization of Au nano-wires in microstructured fibers. *Opt. Express* **2011**, *19*, 12180–12189. [CrossRef] [PubMed]

45. Boehm, J.; François, A.; Ebendorff-Heidepriem, H.; Monro, T.M. Chemical deposition of silver for the fabrication of surface plasmon microstructured optical fibre sensors. *Plasmonics* **2011**, *6*, 133–136. [CrossRef]

46. Lee, H.W.; Schmidt, M.A.; Russel, P.S.J. Excitation of a nanowire "molecule" in gold-filled photonic crystal fiber. *Opt. Lett.* **2012**, *37*, 2946–2948. [CrossRef]

47. Li, B.Y.; Sheng, Z.C.; Wu, M.; Liu, X.Y.; Zhou, G.Y.; Liu, J.T.; Hou, Z.Y.; Xia, C.M. Sensitive real-time monitoring of refractive indices and components using a microstructure optical fiber microfluidic sensor. *Opt. Lett.* **2018**, *43*, 5070–5073. [CrossRef]

48. Li, B.Y.; Wu, M.; Liu, X.Y.; Zhou, G.Y.; Liu, J.T.; Hou, Z.Y.; Xia, C.M. Surface plasmon resonance on the v-type microstructured optical fiber embedded with dual copper wires. *Plasmonics* **2019**, *14*, 383–387. [CrossRef]

49. Paul, B.K.; Khalek, M.A.; Chakma, S.; Ahmed, K. Chalcogenide embedded quasi photonic crystal fiber for nonlinear optical applications. *Ceram. Int.* **2018**, *44*, 18955–18959. [CrossRef]

50. Li, B.; Cheng, T.L.; Chen, J.X.; Yan, X. Graphene-enhanced surface plasmon resonance liquid refractive index sensor based on photonic crystal fiber. *Sensors* **2019**, *19*, 3666. [CrossRef]

51. Younis, B.M.; Heikal, A.M.; Hameed, M.F.O.; Obayya, S.S.A. Highly wavelength-selective asymmetric dual-core liquid photonic crystal fiber polarization splitter. *J. Opt. Soc. Am. B* **2018**, *35*, 1020–1028. [CrossRef]

52. Qu, Y.W.; Yuan, J.H.; Zhou, X.; Li, F.; Yan, B.B.; Wu, Q.; Wang, K.R.; Sang, X.Z.; Long, K.P.; Yu, C.X. Surface plasmon resonance-based silicon dual-core photonic crystal fiber polarization beam splitter at the mid-infrared spectral region. *J. Opt. Soc. Am. B* **2020**, *37*, 2221–2230. [CrossRef]

53. Chiang, J.S.; Sun, N.H.; Lin, S.C.; Liu, W.F. Analysis of an ultrashort PCF-based polarization splitter. *J. Lightw. Technol.* **2010**, *28*, 707–713. [CrossRef]

54. Li, J.H.; Wang, J.Y.; Wang, R.; Liu, Y. A novel polarization splitter based on dual-core hybrid photonic crystal fibers. *Opt. Laser Technol.* **2011**, *43*, 795–800. [CrossRef]

55. Liu, Q.; Li, S.G.; Fan, Z.K.; Zhang, W.; Zi, J.C.; Li, H. Numerical analysis of high extinction ratio photonic crystal fiber polarization splitter based on ZnTe glass. *Opt. Fiber Technol.* **2015**, *21*, 193–197. [CrossRef]

56. Paul, B.K.; Ahmed, K. Si_7N_3 material filled novel heptagonal photonic crystal fiber for laser applications. *Ceram. Int.* **2019**, *45*, 1215–1218. [CrossRef]

57. Ahmed, K.; Paul, B.K.; Jabin, M.A.; Biswas, B. FEM analysis of birefringence, dispersion and nonlinearity of graphene coated photonic crystal fiber. *Ceram. Int.* **2019**, *45*, 15343–15347. [CrossRef]

58. Hui, Z.Q.; Zhang, Y.K.; Soliman, A.H. Mid-infrared dual-rhombic air hole $Ge_{20}Sb_{15}Se_{65}$ chalcogenide photonic crystal fiber with high birefringence and high nonlinearity. *Ceram. Int.* **2018**, *44*, 10383–10392. [CrossRef]